Composite microstructures and piezoelectric properties in tantalum substituted lead-free K 0.5 Na 0.5 Nb 1-x Ta x O 3 ceramics

Florian Jean, Frédéric Schoenstein, Mustapha Zaghrioui, Micka Bah, Pascal Marchet, Julien Bustillo, Fabien Giovannelli, I. Monot-Laffez

Composite microstructures and piezoelectric properties in tantalum substituted lead-free $K_{0.5}Na_{0.5}Nb_{1-x}Ta_xO_3$ ceramics.

F. Jean[1], F. Schoenstein[2], M. Zaghrioui[1], M. Bah[1], P. Marchet[3], J. Bustillo[1], F. Giovannelli[1], I. Monot-Laffez[1*]

[1] *Laboratoire GREMAN UMR 7347, Université de Tours - CNRS - INSA-CVL, IUT de BLOIS 15 rue de la chocolaterie, CS 32903, 41029 Blois Cedex, France.*

[2] *Laboratoire des Sciences des Procédés et des Matériaux, CNRS - LSPM – UPR 3407, Université Paris 13, Sorbonne Paris Cité, 99 Avenue J.B. Clément, 93430 Villetaneuse, France.*

[3] *Université de Limoges, CNRS, IRCER, UMR 7315, Centre Européen de la Céramique, 12 Rue Atlantis, 87068 Limoges Cedex, France.*

[*]*Corresponding author: Isabelle Monot-Laffez*

Email address: isabelle.laffez@univ-tours.fr

Abstract

$K_{0.5}Na_{0.5}Nb_{1-x}Ta_xO_3$ (KNNT) (with x = 0.00, 0.05, 0.10, 0.20, 0.30, 0.50 and 1) ceramics are prepared by ball milling and two calcinations at 830 °C for 5 hours. Subsequent sintering of centimeter size pellets, 1-2 mm thick, is studied using conventional and spark plasma sintering techniques with various conditions. X-Ray diffraction and Raman spectroscopy phase identification reveal orthorhombic to tetragonal phase transitions occurring at about x = 0.50, associated to chemical disorder. Scanning

electron microscope observations and associated energy dispersive X-ray spectroscopy analysis reveal some composite aspect of the ceramics. Substitution of niobium by tantalum, corresponding to x increase, decreases significantly the grain size but also the densification of the ceramics sintered by conventional sintering, while, enhancement of the piezoelectric properties is observed for both sintering techniques. Thanks to parameters optimization of the spark plasma sintering process, temperature-time-pressure, significant improvement of the relative density over 96 %, is obtained for all the compositions sintered between 920 and 960 °C, under 50 MPa, for 5 to 10 minutes with heating rates of 100° C/min. High relative permittivity (ε_r = 1027), piezoelectric charge coefficient (d_{33} = 160 pC/N) and piezoelectric coupling factor (k_p = 46 %) are obtained in spark plasma sintered $K_{0.5}Na_{0.5}Nb_{1-x}Ta_xO_3$ composite ceramics, for x ranging between 0.10 and 0.30 and for some specific spark plasma sintering conditions. Thus, tantalum single element substitution on niobium site, combined with spark plasma sintering, is revealed to be a powerful combination for the optimization and the reliability of piezoelectric properties in KNN system.

KEYWORDS: A. Spark plasma sintering / B. Composite ceramics, Spectroscopy / C. Piezoelectric properties /D. Perovskites / Tantalum

1. Introduction

Lead zirconate titanate (PZT) based piezoceramics are widely used in industry as actuators, sensors, transducers and in other electromechanical devices thanks to their excellent piezoelectric properties. However, the lead contained in these materials is a real issue because of its high toxicity for human health and environment, which lead to its ban by the European Union in 2003 [1]. Since that time, many works focused on the development of new lead-free piezoelectric materials with properties equivalent to those of PZT for target applications. Among the different new lead-free materials, the sodium and potassium niobate $K_{0.5}Na_{0.5}NbO_3$ (KNN) seems to be an interesting alternative, since Saito *et al.* published high piezoelectric performances obtained for textured KNN ceramics doped with lithium, tantalum and antimony of global composition $(Li,Na,K)(Nb,Ta,Sb)O_3$ [2]. Among the abundant literature following these results, many dopings of this composition were published [3,4]. On the other hand, ultrasonic transducers made of pure KNN were recently elaborated in our group, showing the possibility to use this material for concrete applications [5].

In order to improve the piezoelectric properties in KNN system, Ba, Ca, Sr, Zr, Ti or Co doping [6–9] were reported as improving the piezoelectric charge coefficient d_{33} (pC/N or pm/V), which quantifies the volume change when a piezoelectric material is subjected to an electric field or the polarization on application of a stress, the relative permittivity ε_r and the associated electric losses represented by tanδ. But, in most cases, KNN is substituted by the combination of different chemical elements. The substitution of KNN with $Bi_{0.5}(Na_{0.7}K_{0.2}Li_{0.1})_{0.5}TiO_3$ combined with manganese doping leads to the coexistence of orthorhombic and tetragonal phases near room

temperature generating enhanced piezoelectric properties [10]. In the same way, the substitution of KNN with $(Bi_{0.5}Na_{0.5})ZrO_3$ induce a mixture of both rhombohedral–orthorhombic and orthorhombic–tetragonal phase boundaries increasing k_p, d_{33} and curie temperature values. Furthermore, by adding zinc oxide to this compound, grains become smaller and more homogeneous, allowing a decrease of tanδ [11]. Finally, the substitution of KNN with Bi, Sc, Ti and Mn leads to ceramics with a more homogeneous grain size and higher density presenting higher piezoelectric and pyroelectric properties [12,13].

The present work develops the study of the effect of niobium substitution by single element tantalum on the microstructure and piezoelectric properties of $K_{0.5}Na_{0.5}Nb_{1-x}Ta_xO_3$ ceramics sintered by (i) conventional sintering and (ii) spark plasma sintering technique; this latter associates low temperature and high pressure, in a confined environment, which are effective conditions to avoid alkali volatilization and grain coarsening, easily occurring in KNN system, and thus to carefully control the microstructure and composition. Moreover, most of the literature on KNN system does not consider single element doping or substitution and multiple substitutions can lead to versatile properties and difficulties to get a reproducible process, if one considers the future exploitation of this material. In this study, tantalum is chosen because of its ionic radius very close to that of niobium, in order to ensure the substitution and site in the perovskite lattice. In addition, tantalum presents interesting grain growth inhibitor properties [14]. Indeed, Bah *et al.* have highlighted the impact of a fine and homogeneous grain size on pure KNN densification and properties [15].

For what concern tantalum doping, the inspection of the literature shows in several studies that this element is generally combined with lithium and antimony [16–19], showing morphotropic phase boundary and improved piezoelectric properties. Other elements such as lithium [20–22], iron [23] or zirconium and barium [24] are also added to tantalum in order to improve the density and the microstructure leading to enhanced piezoelectric properties of KNN.

The effects of tantalum as single doping element on niobium site was studied on thin films [25,26], single crystal [27–29] and bulk ceramics [30–32]. Concerning bulk ceramics, Chen *et al.* prepared Ta doped KNN ceramics from a powder obtained with a two-stage microwave hydrothermal process. They managed to reach a d_{33} value of 233 pC/N attributed to tantalum and to the morphology of their powders obtained with this process [30]. For their part, Hussain *et al.* synthesized sodium excess and Ta-modified $(K_{0.470}Na_{0.545})(Nb_{0.55}Ta_{0.45})O_3$ textured ceramics by a reactive templated grain growth method. They observed an increase of 44 % for the d_{33} value compared to non-textured ceramics [31]. Finally, Lv *et al.* prepared tantalum doped KNN by the solid-state reaction technique. Their best results in terms of d_{33}, k_p and ε' at 1 kHz are 205 pC/N, 45 % and 967 respectively, obtained for a substitution of niobium by 30 mol% of tantalum with a densification of 94 %, while k_t decreased with increasing the tantalum content [32]. In order to increase the relative density of KNN doped with tantalum, sintering aids such as CuO [33,34], LiF [35] or ZnO [36] were also used. Another way to reach high density for KNN based ceramics is the use of alternative sintering techniques such as hot pressing [37], flash sintering [38] or spark plasma sintering [39,40]. This latter may allow reaching high density without grain coarsening, thus keeping the benefit of Ta as grain growth inhibitor. Thus, the aim of the present work

is to study the effects of niobium substitution by tantalum in $K_{0,5}Na_{0,5}Nb_{1-x}Ta_xO_3$ on the structure, the microstructure and the piezoelectric properties of ceramics sintered by spark plasma sintering techniques and then to compare the benefits of such microstructure with the same ceramics elaborated by conventional sintering process.

2. Material and methods

$K_{0.5}Na_{0.5}Nb_{1-x}Ta_xO_3$ (KNNT) (with x = 0.00, 0.05, 0.10, 0.20, 0.30, 0.50 and 1) powders are prepared by the conventional solid-state reaction technique. Oxide and carbonate powders of K_2CO_3 (99+ %, ChemPUR), Na_2CO_3 (99.9+ %, ChemPUR), Nb_2O_5 (99.9 %, ChemPUR) and Ta_2O_5 (99.9 % ChemPUR) are used as starting materials. The raw powders are first dried at 200 °C during 4 h, weighted in stoichiometric ratios and then mixed during 15 min at 400 rpm in an agate grinding bowl with agate balls. The resulting mixtures are calcined at 830 °C for 5 h. After the first calcination, these powders are milled again and calcined a second time at 830 °C for 5 h. After both calcinations, ceramic pellets are sintered using two different techniques: conventional sintering and spark plasma sintering. For conventional sintering, the powders are uniaxially pressed into 12 mm in diameter and 2 mm thick disks, under 170 MPa, using polyvinyl alcohol (PVA) as a binder. The pellets are then sintered in a tubular furnace under air at 1120 °C for 10 h with a heating rate of 3 °C/min. For spark plasma sintering, SPS Syntex 515S (FUJI) equipment is used. 2.5 g of calcined powders are inserted in a 15 mm diameter graphite die, and placed between two graphite electrodes. The system is then submitted to a heating cycle combined with a pressure cycle. Uniaxial pressures from 20 to 200 MPa can be applied on the graphite die.

Several sintering parameters, under argon atmosphere, are studied: heating rates (50 ° and 100 °C/min), dwell temperatures (920, 940, 960 and 980 °C), dwell times (5 and 10 min), and pressure conditions (50 and 200 MPa). After spark plasma sintering, the samples are annealed under oxygen flow at 900 °C for 1 hour using heating rate 300 °C/h from room temperature to 600 °C and then 50 °C/h from 600 to 900 °C; the cooling rate was 300 °C/h. This thermal treatment allows to recover full oxygen content, and to burn out carbon contamination from the die. All the pellets are then polished to obtain a thickness of 1 mm with parallel surfaces for the piezoelectric characterizations. Phase identification of the ceramics is carried out by X-ray diffraction with a Cu-K_α radiation filtered by Ni (BRUKER D8 X-Ray diffractometer) equipped with a high performance linear detector, between 20 ° and 80 °, with a 0,02 ° step and 1 s exposition time, equivalent to 192 s for a point detector. Rietveld refinements are performed using FullProf program [41]. The fitting procedure consists in refining the cell parameters, then atomic positions. Then (Na, K) and (Nb,Ta) are assigned to the same site respectively, and defined as randomly distributed. The ratio between Na and K, and the ratio between Nb and Ta have been fixed to the nominal compositions respectively.

Raman spectroscopy is performed at room temperature on sintered samples surfaces using Renishaw Invia spectrometer. A 514 nm argon laser is used as an excitation with a power of 1 W focused by X 50 lens. The relative densities of the different samples are measured by geometrical and weight measurements, and referring to the theoretical density, calculated from Rietveld refinements. Microstructure and compositions are checked on polished surfaces, with scanning electron microscopy (FEI – Quanta200 and TESCAN-MIRA 3 SEM) coupled with energy-

dispersive X-ray spectroscopy analysis (EDS - Oxford Inca X-act). Due to low energy of oxygen, its quantification is very much challenging; thus for this ABO_3 perovskite system, the number of oxygen atoms is assumed to be 3 for all the compositions and the quantification of elements is calculated on the cations.

To perform electrical measurements, high purity silver paint (SPI supplies) is pasted on both sides of the pellets and fired at 900 °C for 20 min for the adhesion of the electrodes. All samples are then poled at 130 °C in oil under 3 kV/mm for 10 min using a DC power supply and cooled to room temperature under electrical field. The complex electrical impedance is then measured according to frequency, using a Vector Network Analyzer (Omicron Lab Bode 100). The planar coupling factor k_p is calculated by the resonance-antiresonance method on the basis of IEEE standards on Piezoelectricity [42]. Relative permittivity (ε_r) and dielectric losses (tanδ) are measured at 1 kHz using a precision impedance analyzer (Agilent 4294A). Piezoelectric coefficients are measured with a Berlincourt -d_{33} - meter (Piezotest PM-200).

3. Results and discussion

3.1 Structural aspects

Fig. 1 presents the X-ray diffraction patterns of all the $K_{0.5}Na_{0.5}Nb_{1-x}Ta_xO_3$ compositions, corresponding to the conventionally sintered ceramics at 1120 °C for 10 h. Note that the analysis of the XRD diagrams of SPS-sintered samples leads to exactly the same observations and conclusions.

For the two $K_{0.5}Na_{0.5}Nb_{1-x}Ta_xO_3$ end members (x = 0) and KNT (x = 1), X-Ray diffraction patterns are consistent with previous studies of Ishizawa *et al.* [43] and with JCPDS $K_{0.5}Na_{0.5}NbO_3$ reference [44]. KNN (x = 0) is found to crystallize in orthorhombic structure with *Amm2* space group, while KNT (x = 1) crystallizes in cubic structure with *Pm-3m* space group. With increasing Ta content x from pure KNN to pure KNT, three changes can be observed, as shown in inset of Fig. 1. The structural evolution is clearly observed around $2\theta = 45$ ° on the (202) and (020) diffraction peaks of the orthorhombic phase. Between x = 0 and x = 0.10, the peak positions do not significantly change, with a very small peak shift, indicating a small cell volume variation. For x = 0.20 and 0.30, the peaks shift is accentuated and both peaks become closer, suggesting a reduction of the orthorhombic distortion, i.e. the structure evolves towards tetragonal or cubic. Finally for x = 0.50, the two previous peaks have nearly merged and might correspond to (200) and (020) diffraction peaks of a tetragonal structure.

In order to quantify these evolutions, Rietveld refinements are performed on the diffraction patterns. For x = 0, 0.05, 0.10, 0.20 and 0.30, the structure is correctly described by the orthorhombic *Amm2* symmetry. For x = 1 (KNT), experimental XRD data are well described by the cubic *Pm-3m* phase. For x = 0.5, both orthorhombic and cubic structures are tested. As a result, orthorhombic phase describes better the experimental data, but “a” and “c” cell parameters are found to be very close, strongly suggesting *P4bm* tetragonal phase, rather than the orthorhombic one [45].

Obtained cell parameters are plotted in Fig. 2 as a function of the increasing amount of Ta, and according to a pseudo cubic cell (i.e. $a_c = a_O$, $b_c = b_O / \sqrt{2}$, $c_c = c_O / \sqrt{2}$

for the orthorhombic *Amm2* samples). One can observe that at least three domains can be identified and the structure evolution of $K_{0.5}Na_{0.5}Nb_{1-x}Ta_xO_3$ composition undergoes orthorhombic to tetragonal transition between x = 0.30 and x = 0.50 and then a cubic transition for x = 1.

These results confirm that tantalum is effectively incorporated in the KNNT ceramics, all along the substitution but not in a continuous process. It can be noticed also that when increasing the tantalum amount until x = 0.50, all diffraction peaks become broader and this can be attributed to chemical disorder and possibly to the presence of smaller crystallites, in accordance with the grain growth inhibitor role of tantalum.

In order to confirm and complete the X-Ray diffraction analyses, Raman spectroscopy is performed on all the samples and compositions and the spectra are presented in Fig. 3a.

For the end members x = 0 and x = 1, Raman spectra are consistent with the literature [46-52]. For x = 1, $K_{0.5}Na_{0.5}TaO_3$ (KNT) crystallizes in a cubic structure with *Pm-3m* space group, which must not present any active Raman mode. However, the spectrum presents some peaks that might be attributed to second order Raman modes or even infrared modes, activated by some structural disorder [53-54]. For x = 0, the observed Raman spectrum is similar to that reported by several authors [46] for KNN and related compositions, and corresponds to the orthorhombic structure with *Amm2* space group [46-52, 55-58].. This spectrum can be described by means of internal vibrations of the octahedral NbO_6 (O_h symmetry). As well known, the A_{1g} (ν_1) and E_g

(ν_2) modes correspond to a symmetrical and asymmetrical stretching vibrations; and T_{2g} (ν_5) mode is related to a symmetrical bending vibration [47-49,51-52].

The spectrum evolution between x = 0 and x = 0.5 shows that the high frequency modes at 600 cm^{-1} and 850 cm^{-1} wavenumbers are not significantly shifted or modified in their shape with the increasing substitution of niobium by tantalum. For what concerns the low wavenumbers modes around 200-300 cm^{-1} a significant evolution can be observed. For x = 0.05 and x = 0.10 the spectra are similar to that of x = 0, corresponding to an orthorhombic structure, in accordance with XRD results. For x = 0.20 and x = 0.30, these two spectra present a real difference with the previous ones. Indeed, the mode numbers still correspond to an orthorhombic structure but their intensities are different. This result is also consistent with the evolution of XRD diagrams and the cell parameters (Figs. 1 and 2). For x = 0.50, the number, the intensity and the positions of the peaks are clearly different from the previous ones and do not correspond to a cubic *Pm-3m* structure; the environment, thus modified, can correspond to a tetragonal structure, as was found in the Rietveld analysis.

Structural phase transition in perovskite is often identified by means of the band shift of some selected modes. For KNN and related compositions, wavenumber of A_{1g} (ν_1) and E_g (ν_2) modes in the region 500 - 700 cm^{-1} were largely used to identify phase transitions [47-49,51,52,59]. Hence, both band modes were fitted to the sum of two Gaussian-Lorentzian curves and wavenumbers versus tantalum content is plotted in figs. 3b and 3c. One can observe a discontinuous change in wavenumbers versus tantalum content, notably the shift of both modes to higher wavenumbers. This feature can be attributed to the structural phase transition from orthorhombic

structure (*Amm2*) to tetragonal structure (*P4bm*). Also note that E_g (ν_2) mode evolution shows two behaviors between x = 0 and 0.3 (Fig. 3b), with a slight increase in the wavenumber for x = 0 to 0.1 and then a decrease above. These features are in total agreement with the cell parameters evolution obtained from Rietveld analyses.

From these structural and vibrational considerations, it can be concluded that tantalum is successfully introduced in the KNN structure, with the creation of some chemical disorder. Two structural transitions occur with increasing the amount of tantalum, from *Amm2* orthorhombic structure to *P4bm* tetragonal structure above x = 0.30 and finally to *Pm-3m* cubic structure for x = 1 (KNT).

3.2 Microstructural features

Microstructure of KNNT ceramics sintered with the conventional route at 1120 °C for 10 h are shown in Fig. 4. All ceramics present cuboid grains with a bimodal distribution of micron size grains. For x = 0 (Fig. 4a), the first population of grain sizes is centered on 2 µm and the second one is centered on 5-6 µm. With increasing the amount of Tantalum, a drastic decrease of grain size can be observed (Fig. 4b - f). Thus for x = 0.50 (Fig. 4e), grain size ranges from submicrometric to 1 µm values and is similar to x = 1 (KNT, Fig. 4f). Another significant point is the apparent density, which decreases with increasing the amount of tantalum. The use of grain growth inhibitors (like tantalum) is known to inhibit the densification during the sintering step, and is confirmed here by the observations in Fig. 4. The use of tantalum thus allows obtaining ceramics with a micrometric and narrow grain size, which is also confirmed by the

evolution of the diffraction peaks towards slightly broader peaks, which can correspond to smaller domains.

The increase of densification with the use of spark plasma sintering technique is clearly shown in Fig. 5c and 5d, compared to conventional sintering. The results of the relative density measurements, shown in Fig. 6, clearly emphasize the benefit of Spark Plasma Sintering for the sintering of tantalum substituted KNNT, whatever the amount fo Ta.

A relative density over 95 % can be maintained for all the substitution levels in SPS sintered samples, at 920 °C, during 5 minutes and under 50 MPa, while the relative density continuously decreases with the increase of niobium substitution by tantalum in conventionally sintered samples, even by modifying the sintering conditions (times and temperatures). Otherwise, another important feature on these microstructures is the different chemical contrasts that can be detected in these large scale micrographs using backscattered electron detector, for all the substituted samples and whatever the sintering process. A focus on these microstructures is given in the zoom presented Fig. 7. Three kinds of contrast levels appear, homogeneously distributed, consisting in light and dark inclusions embedded into a grey matrix (Fig. 7a). The number of light inclusions increases with the tantalum content, the dark inclusions remaining in the same proportions. Similar observations made for pure KNN (not shown here) point out that this phenomenon does not occur in non-substituted samples, prepared in the same conditions. Thus, KNNT ceramics appear to have a composite microstructural aspect.

To go further, analyzes by energy dispersive X-ray spectroscopy (EDXS) coupled with Scanning electron microscopy (SEM) observations were carried out on spark plasma sintered KNNT ceramics (x = 0.20) corresponding to the microstructures of Fig. 7. On the one hand, it appears light inclusions composed of submicrometric cuboid grains, as shown in Fig. 7b. They are tantalum rich, with a very low amount of niobium and sodium deficient. On the other hand, dark inclusions are made of bigger grains with an average size of 3 to 5 µm, similar to x = 0 grain size, and with less defined shapes; these inclusions are niobium rich and tantalum deficient compared to the nominal composition. The matrix around these two kinds of inclusions (Fig. 7c) suggests a homogeneous mixture of small and coarse grains. Energy dispersive X-Ray spectroscopy analysis shows a ratio of 1:5 between tantalum and niobium, which corresponds to the nominal substitution rate of tantalum for $K_{0.5}Na_{0.5}Nb_{0.8}Ta_{0.2}O_3$ composition. It can also be underlined that the A-site and the B-site occupancy rates of the ABO_3 perovskite are preserved for each analyzed areas, the ratio between (Na + K) and (Nb + Ta) remaining 1 in all cases. Actually, KNNT ceramics prepared in this study appear as a several phases composites. Considering again the XRD analyses presented in the first part of this study, one can consider that tantalum is effectively introduced in the KNN structure forming $K_{0,5}Na_{0,5}Nb_{1-x}Ta_xO_3$ (KNNT) and corresponding to the main phase observed in Raman study. But even for a low value of x, new phases appear rapidly, regularly dispersed at a large scale in the microstructure but also at a lower scale. Thus the dark areas are close to $K_yNa_{1-y}NbO_3$ composition (KNN) and in the form of few micrometers grains, and the light areas correspond nearly to $K_yNa_{1-y}TaO_3$ composition (KNT), constituted of submicrometric to one micrometer grains. These last two phases certainly present very similar diffraction patterns that could not be

differentiated from the whole sample by basic XRD analyzes. To our knowledge, such composite structures have not been reported for tantalum doped KNN. In recent literature on KNN and other related lead-free piezoelectric systems [60] the composite approach is one way to provide chemical disorder, structural strains and distortions, or morphotropic phase boundaries. In polycrystalline ceramics, interfaces and grain-to-grain interactions can also contribute to modify the movement of the domain walls, with a hardening or softening effect [61]. These different microstructural factors can modify electromechanical response upon application of an electric field, and significant improvement in relaxor systems were shown with this approach.

For all these reasons, in the following, the piezoelectric properties are considered in these new composite materials.

3.3 Piezoelectric properties

For what concern the physical properties, for both sintering techniques the piezoelectric coefficients d_{33} are measured and the coupling factors for planar mode k_p, the relative permittivity ε_r and dielectric losses tanδ (at 1 kHz) are deduced from impedance measurements.

As shown in Fig. 8, the substitution of niobium by tantalum clearly impacts the piezoelectric coefficient d_{33}. An increase of this property is observed with the increase of tantalum amount up to x = 0.20-0.30 for both sintering techniques. Note that the increase of d_{33} is more significant for the SPS samples, with the highest value of 160 pC/N for x = 0.30, comparable to the value (159 pC/N) obtained by Lv *et al.* [32] in a 20 mol% substituted KNN.

For what concern the planar electromechanical coupling factor k_p, the conventional sintering appears to improve k_p with the incorporation of tantalum from x = 0.05 until x = 0.10, with a slight decrease above this value. k_p ranges between 23-26 % for x = 0.05 to x = 0.20, and it remains more than two times higher than for the non-substituted samples. With the spark plasma sintering technique, high k_p values are obtained in all cases, compared to conventional sintering, ranging from 42 to 46 % with the optimum value for x = 0.10 but with a low variation until x = 0.20. In the case of SPS sintered sample, the benefit of niobium substitution by tantalum is less sensitive than for conventional sintering. For comparison, the best k_p values obtained by Lv *et al.* are 44.6 % for x = 0.10 and 45 % for x = 0.30, with a low variation with tantalum content as well, similarly to the present study.

The relative permittivity is presented in Fig. 9; with conventional sintering technique, increasing the tantalum content has no impact on the relative permittivity with measured values around 250-300 on the whole range of substitution. Considering the low and decreasing relative density of these samples, often linked to the permittivity values, it seems that a positive effect of tantalum may balance the density losses. However, there is a significant increase of the relative permittivity with both SPS sintering and increase of tantalum amount, reaching a maximum value of ε_r = 805 for x = 0.30. These results highlight the joint benefit of the SPS technique and tantalum incorporation on the ceramics relative densities. Note that the best properties are obtained between x = 0.10 and x = 0.30, which are the compositions corresponding to distorted orthorhombic structure or between orthorhombic and tetragonal structures. This is a complementary proof of the necessity of phase boundaries or morphotropic phases coexistence for the improvement of some piezoelectric properties.

Finally, it can be observed in Fig. 9 that the dielectric losses remain under a value of 3 % for most of the samples, slightly increasing above 4 % for x = 0.30 and x = 0.50 in the case of SPS sintered samples.

3.4 SPS parameters considerations

To go further, the impact of spark plasma sintering conditions on electrical properties is studied for the KNNT ceramics with x = 0.20, corresponding to the optimum of all the properties. The studied sintering parameters are the temperature, the heating rate, the dwell time and the pressure. The results are summarized Table 1.

Using the sintering parameters corresponding to the above results (100 °C/min, 5 min dwell time and 50 MPa uniaxial pressure), the temperature is varied from 920 to 980 °C. As expected, it appears that the density of the ceramics is strongly influenced by the sintering temperature. It significantly increases with the increase of the temperature up to a maximum of 94 % densification, reached at 960 °C. The samples relative densities remain an important characteristic, because all the samples with the lowest densities undergo electrical breakdown during the poling step. Considering 960 °C as the optimal sintering temperature value, ramp speed and dwell time are varied. Decreasing the ramp speed to 50 °C/min depresses the density, while increasing the dwell time, from 5 to 10 min, allows reaching the highest relative density of 96.3 %. High coupling factor k_p and piezoelectric coefficient d_{33} are obtained for this sample with values of 42.3 % and 155 pC/N, respectively, associated to low dielectric losses (2.86 %). According to these results, it is confirmed that the evolution of d_{33} values is closely linked to the evolution of the samples density. Finally, the pressure parameter

was increased from 50 to 200 MPa for one sample. Under 200 MPa at 920 °C for 5 minutes, a relative density of 92.3 % is obtained, which represents an increase of 30 % of the relative density compared to the same composition sintered under 50 MPa. This result shows the strong influence of the pressure on the densification during SPS process. Moreover, this sample presents the highest relative permittivity with a value of 1027, highlighting the benefit of the SPS technique on this property and confirming the results of Fig. 9. Indeed, compared to the value obtained for the sample with the same composition, sintered by conventional sintering, the relative permittivity is multiplied by a factor of five and is higher than that obtained by many research groups in KNN-system ceramics. To conclude on the results summarized in Table 1, SPS sintering techniques appears to be a powerful way to produce highly densified $K_{0,5}Na_{0,5}Nb_{1-x}Ta_xO_3$ ceramics with improved piezoelectric properties. Indeed, thanks to SPS technique, in x = 0.20 KNNT, relative permittivity higher than 900, K_p value over 40 % and piezoelectric coefficient d_{33} over 135 and up to 155 pC/N can be achieved and maintained.

4. Conclusion

$K_{0.5}Na_{0.5}Nb_{1-x}Ta_xO_3$ (KNNT) (with x = 0.00, 0.05, 0.10, 0.20, 0.30, 0.50 and 1) ceramics were sintered by conventional and spark plasma sintering techniques. X-Ray diffraction and Raman analyses confirmed tantalum incorporation in KNN perovskite with the appearance of some chemical disorder with increasing substitution. Two structural transitions are evidenced, from orthorhombic to tetragonal between x = 0.30 and x = 0.50 and from tetragonal to cubic for x = 1 ($K_{0.5}Na_{0.5}TaO_3$). Scanning electron

microscopy observations and energy dispersive X-ray spectroscopy analyses evidenced a composite microstructure of the ceramics with tantalum rich and niobium rich inclusions into a $K_{0.5}Na_{0.5}Nb_{1-x}Ta_xO_3$ matrix of the expected composition. However, this composite microstructure is not detrimental and tantalum incorporation in $K_{0.5}Na_{0.5}Nb_{1-x}Ta_xO_3$ has a beneficial effect on piezoelectric properties. In order to balance the difficulty to densify the KNNT ceramics, the use of the spark plasma sintering techniques enables to obtain highly densified substituted ceramics, 94 to 96 % of relative density, with a significant impact of the sintering temperature and pressure on the density. With different optimized sintering parameters, interesting piezoelectric properties are obtained: k_p = 46 %, d_{33} = 155 pC/N, ε_r = 1027. The cross influence of the different SPS parameters on piezoelectric properties is revealed here and the values of K_p and ε_r are potentially interesting for the use of this material in transducer's element or energy harvesting devices for applications [62], preparing thus the "after PZT" devices.

Acknowledgments:

This work was supported by "Région Centre Val de Loire, France" in K-NNOPEE project (Contract N°20140091661).

REFERENCES:

[1] European Union, Directive 2002/95/EC of the European Parliament and of the Council of 27 January 2003 on the restriction of the use of certain hazardous substances in electrical and electronic equipment, Off. J. Eur. Union. 46 (2003) 19–23.

[2] Y. Saito, H. Takao, T. Tani, T. Nonoyama, K. Takatori, T. Homma, T. Nagaya, M. Nakamura, Lead-free piezoceramics, Nature. 432 (2014) 84–87. doi:10.1038/nature03028.

[3] F. Rubio-Marcos, J.J. Romero, J.F. Fernández, P. Marchet, Control of the crystalline structure and piezoelectric properties of (K,Na,Li)(Nb,Ta,Sb)O_3 ceramics through transition metal oxide doping, Appl. Phys. Express. 4 (2011) 101501. doi:10.1143/APEX.4.101501.

[4] G. Lévêque, P. Marchet, F. Levassort, L.P. Tran-Huu-Hue, J.R. Duclere, Lead free (Li,Na,K)(Nb,Ta,Sb)O_3 piezoelectric ceramics: influence of sintering atmosphere and ZrO_2 doping on densification, microstructure and piezoelectric properties, J. Eur. Ceram. Soc. 31 (2011) 577–588. doi:10.1016/j.jeurceramsoc.2010.10.031.

[5] M. Bah, F. Giovannelli, F. Schoenstein, C. Brosseau, J.-R. Deschamps, F. Dorvaux, L. Haumesser, E. Le Clezio, I. Monot-Laffez, Ultrasonic transducers based on undoped lead-free $(K_{0.5}Na_{0.5})NbO_3$ ceramics, Ultrasonics. 63 (2015) 23–30. doi:10.1016/j.ultras.2015.06.007.

[6] J. Taub, L. Ramajo, M.S. Castro, Phase structure and piezoelectric properties of Ca- and Ba-doped $K_{1/2}Na_{1/2}NbO_3$ lead-free ceramics, Ceram. Int. 39 (2013) 3555–3561. doi:10.1016/j.ceramint.2012.10.181.

[7] B. Malic, J. Bernard, J. Holc, D. Jenko, M. Kosec, Alkaline-earth doping in (K,Na)NbO_3 based piezoceramics, J. Eur. Ceram. Soc. 25 (2005) 2707–2711. doi:10.1016/j.jeurceramsoc.2005.03.127.

[8] X. Vendrell, J.E. García, X. Bril, D.A. Ochoa, L. Mestres, G. Dezanneau, Improving the functional properties of $(K_{0.5}Na_{0.5})NbO_3$ piezoceramics by acceptor doping, J. Eur. Ceram. Soc. 35 (2015) 125–130. doi:10.1016/j.jeurceramsoc.2014.08.033.

[9] G.-Z. Zang, X.-J. Yi, J. Du, Y.-F. Wang, Co_2O_3 doped $(Na_{0.65}K_{0.35})NbO_3$ piezoceramics, Mater. Lett. 64 (2010) 1394–1397. doi:10.1016/j.matlet.2010.03.036.

[10] D. Lin, D. Huang, Q. Zheng, Structure, dielectric and piezoelectric properties of $K_{0.5}Na_{0.5}NbO_3$–$Bi_{0.5}(Na_{0.7}K_{0.2}Li_{0.1})_{0.5}TiO_3$ ceramics, J. Phys. Chem. Solids. 74 (2013) 1021–1025. doi:10.1016/j.jpcs.2013.02.023.

[11] F. Li, D. Xiao, J. Wu, Z. Wang, C. Liu, J. Zhu, Phase structure and electrical properties of $(K_{0.5}Na_{0.5})NbO_3$–$(Bi_{0.5}Na_{0.5})ZrO_3$ lead-free ceramics with a sintering aid of ZnO, Ceram. Int. 40 (2014) 14601–14605. doi:10.1016/j.ceramint.2014.06.045.

[12] X.P. Jiang, Y. Chen, K.H. Lam, S.H. Choy, J. Wang, Effects of MnO doping on properties of $0.97K_{0.5}Na_{0.5}NbO_3$–$0.03(Bi_{0.5}K_{0.5})TiO_3$ piezoelectric ceramics, J. Alloys Compd. 506 (2010) 323–326. doi:10.1016/j.jallcom.2010.06.200.

[13] X. Li, M. Jiang, J. Liu, J. Zhu, X. Zhu, J. Zhu, D. Xiao, Enhanced piezoelectric properties in Mn-doped $0.98K_{0.5}Na_{0.5}NbO_3$–$0.02BiScO_3$ lead-free ceramics, J. Am. Ceram. Soc. 92 (2009) 1625–1628. doi:10.1111/j.1551-2916.2009.03090.x.

[14] T.M. Harkulich, J. Magder, M.S. Vukasovich, R.J. Lockhart, Ferroelectrics of ultrafine particle size: II, grain growth inhibition studies, J. Am. Ceram. Soc. 49 (1966) 295–299. doi:10.1111/j.1151-2916.1966.tb13266.x.

[15] M. Bah, F. Giovannelli, F. Schoenstein, G. Feuillard, E. Le Clezio, I. Monot-Laffez, High electromechanical performance with spark plasma sintering of undoped $K_{0.5}Na_{0.5}NbO_3$ ceramics, Ceram. Int. 40 (2014) 7473–7480. doi:10.1016/j.ceramint.2013.12.097.

[16] D. Lin, K.W. Kwok, H.L.W. Chan, Phase structures and electrical properties of $K_{0.5}Na_{0.5}(Nb_{0.925}Ta_{0.075})O_3$–$LiSbO_3$ lead-free piezoelectric ceramics, J. Phys. D: Appl. Phys. 40 (2007) 6060. doi:10.1088/0022-3727/40/19/044.

[17] J. Wu, T. Peng, Y. Wang, D. Xiao, J. Zhu, Y. Jin, J. Zhu, P. Yu, L. Wu, Y. Jiang, Phase structure and electrical properties of $(K_{0.48}Na_{0.52})(Nb_{0.95}Ta_{0.05})O_3$-$LiSbO_3$ lead-free piezoelectric ceramics, J. Am. Ceram. Soc. 91 (2008) 319–321. doi:10.1111/j.1551-2916.2007.02102.x.

[18] S. Qian, K. Zhu, X. Pang, J. Liu, J. Qiu, J. Du, Phase transition, microstructure, and dielectric properties of Li/Ta/Sb co-doped (K, Na)NbO_3 lead-free ceramics, Ceram. Int. 40 (2014) 4389–4394. doi:10.1016/j.ceramint.2013.08.110.

[19] F. Rubio-Marcos, P. Marchet, T. Merle-Méjean, J.F. Fernandez, Role of sintering time, crystalline phases and symmetry in the piezoelectric properties of lead-free KNN-modified ceramics, Mater. Chem. Phys. 123 (2010) 91–97. doi:10.1016/j.matchemphys.2010.03.065.

[20] J.-J. Zhou, J.-F. Li, K. Wang, X.-W. Zhang, Phase structure and electrical properties of (Li,Ta)-doped (K,Na)NbO_3 lead-free piezoceramics in the vicinity of Na/K = 50/50, J. Mater. Sci. 46 (2011) 5111–5116. doi:10.1007/s10853-011-5442-7.

[21] Y. Zhen, J.-F. Li, Normal sintering of (K,Na)NbO_3-based ceramics: influence of sintering temperature on densification, microstructure, and electrical properties, J. Am. Ceram. Soc. 89 (2006) 3669–3675. doi:10.1111/j.1551-2916.2006.01313.x.

[22] E. Hollenstein, M. Davis, D. Damjanovic, N. Setter, Piezoelectric properties of Li- and Ta-modified $(K_{0.5}Na_{0.5})NbO_3$ ceramics, Appl. Phys. Lett. 87 (2005) 182905. doi:10.1063/1.2123387.

[23] H. Li, W. Yang, Y. Li, Q. Meng, Z. Zhou, Room-temperature magnetocapacitance in Fe-doped $K_{0.5}Na_{0.5}Nb_{0.95}Ta_{0.05}O_3$ ceramics, Appl. Phys. Express. 5 (2012) 101501. doi:10.1143/APEX.5.101501.

[24] B. Zhang, J. Wu, X. Wang, X. Cheng, J. Zhu, D. Xiao, Rhombohedral–orthorhombic phase coexistence and electrical properties of Ta and $BaZrO_3$ co-modified (K, Na)NbO_3 lead-free ceramics, Curr. Appl. Phys. 13 (2013) 1647–1650. doi:10.1016/j.cap.2013.06.010.

[25] S.Y. Lee, C.W. Ahn, J.S. Kim, A. Ullah, H.J. Lee, H.-I. Hwang, J.S. Choi, B.H. Park, I.W. Kim, Enhanced piezoelectric properties of Ta substituted-($K_{0.5}Na_{0.5}$)NbO_3 films: a candidate for lead-free piezoelectric thin films, J. Alloys Compd. 509 (2011) L194–L198. doi:10.1016/j.jallcom.2011.03.031.

[26] S.Y. Lee, J.S. Kim, C.W. Ahn, A. Ullah, H.J. Lee, I.W. Kim, Influence of piezoelectric property on annealing temperature of Ta-substituted ($K_{0.5}Na_{0.5}$)NbO_3 thin films by chemical solution deposition, Curr. Appl. Phys. 11 (2011) S157–S160. doi:10.1016/j.cap.2011.01.032.

[27] L. Zheng, X. Huo, R. Wang, J. Wang, W. Jiang, W. Cao, Large size lead-free (Na,K)(Nb,Ta)O_3 piezoelectric single crystal: growth and full tensor properties, CrystEngComm. 15 (2013) 7718–7722. doi:10.1039/C3CE40658J.

[28] T. Hattori, Y. Kitanaka, Y. Noguchi, M. Miyayama, Growth and ferroelectric/piezoelectric properties of (K,Na)(Nb,Ta)O_3 ferroelectric single crystals, Key Eng. Mater. 566 (2013) 64–67. doi:10.4028/www.scientific.net/KEM.566.64.

[29] M. Bah, F. Giovannelli, R. Retoux, J. Bustillo, E.L. Clezio, I. Monot-Laffez, Crystal growth and piezoelectric properties of lead-free based $K_{0.5}Na_{0.5}NbO_3$ by the floating zone method, Cryst. Growth Des. 16 (2016) 315–324. doi:10.1021/acs.cgd.5b01271.

[30] L. Chen, G. Qiu, B. Peng, M. Guo, M. Zhang, ($K_{0.5}Na_{0.5}$)($Nb_{1-x}Ta_x$)O_3 ceramics with a higher d_{33}: preparation from a two-stage microwave hydrothermal process, Ceram. Int. 41 (2015) 13331–13340. doi:10.1016/j.ceramint.2015.07.117.

[31] A. Hussain, A. Maqbool, J.S. Kim, T.K. Song, M.H. Kim, W.J. Kim, S.S. Kim, Sodium excess Ta-modified ($K_{0.5}Na_{0.5}$)NbO_3 ceramics prepared by reactive template grain growth method, Int. J. Appl. Ceram. Technol. 12 (2015) 228–234. doi:10.1111/ijac.12150.

[32] Y.G. Lv, C.L. Wang, J.L. Zhang, L. Wu, M.L. Zhao, J.P. Xu, Tantalum influence on physical properties of ($K_{0.5}Na_{0.5}$)($Nb_{1-x}Ta_x$)O_3 ceramics, Mater. Res. Bull. 44 (2009) 284–287. doi:10.1016/j.materresbull.2008.06.019.

[33] M. Matsubara, K. Kikuta, S. Hirano, Piezoelectric properties of $(K_{0.5}Na_{0.5})(Nb_{1-x}Ta_x)O_3-K_{5.4}CuTa_{10}O_{29}$ ceramics, J. Appl. Phys. 97 (2005) 114105. doi:10.1063/1.1926396.

[34] M. Matsubara, T. Yamaguchi, W. Sakamoto, K. Kikuta, T. Yogo, S. Hirano, Processing and piezoelectric properties of lead-free (K,Na) (Nb,Ta) O_3 ceramics, J. Am. Ceram. Soc. 88 (2005) 1190–1196. doi:10.1111/j.1551-2916.2005.00229.x.

[35] J.-J. Zhou, L.-Q. Cheng, K. Wang, X.-W. Zhang, J.-F. Li, H. Liu, J.-Z. Fang, Low-temperature sintering of (K,Na)NbO_3-based lead-free piezoceramics with addition of LiF, J. Eur. Ceram. Soc. 34 (2014) 1161–1167. doi:10.1016/j.jeurceramsoc.2013.11.029.

[36] Y. Watanabe, K. Sumida, S. Yamada, S. Sago, S. Hirano, K. Kikuta, Effect of Mn-doping on the piezoelectric properties of $(K_{0.5}Na_{0.5})(Nb_{0.67}Ta_{0.33})O_3$ lead-free ceramics, Jpn. J. Appl. Phys. 47 (2008) 3556–3558. doi:10.1143/JJAP.47.3556.

[37] R.E. Jaeger, L. Egerton, Hot pressing of potassium-sodium niobates, J. Am. Ceram. Soc. 45 (1962) 209–213. doi:10.1111/j.1151-2916.1962.tb11127.x.

[38] G. Corapcioglu, M.A. Gulgun, K. Kisslinger, S. Sturm, S.K. Jha, R. Raj, Microstructure and microchemistry of flash sintered $K_{0.5}Na_{0.5}NbO_3$, J. Ceram. Soc. Jpn. 124 (2016) 321–328. doi:10.2109/jcersj2.15290.

[39] J.-F. Li, K. Wang, B.-P. Zhang, L.-M. Zhang, Ferroelectric and piezoelectric properties of fine-grained $Na_{0.5}K_{0.5}NbO_3$ lead-free piezoelectric ceramics prepared by spark plasma sintering, J. Am. Ceram. Soc. 89 (2006) 706–709. doi:10.1111/j.1551-2916.2005.00743.x.

[40] F. Delorme, M. Bah, F. Schoenstein, F. Jean, M. Zouaoui Jabli, I. Monot-Laffez, F. Giovannelli, Thermoelectric properties of oxygen deficient $(K_{0.5}Na_{0.5})NbO_3$ ceramics, Mater. Lett. 162 (2016) 24–27. doi:10.1016/j.matlet.2015.09.124.

[41] J. Rodriguez-Carvajal, Recent advances in magnetic structure determination by neutron powder diffraction, Physica B 192 (1993) 55–69.

[42] IEEE Standard on Piezoelectricity (1987), IEEE Standard 176 -1987, Institute of Electrical and Electronic Engineers, New York.

[43] N. Ishizawa, J. Wang, T. Sakakura, Y. Inagaki, K. Kakimoto, Structural evolution of $Na_{0.5}K_{0.5}NbO_3$ at high temperatures, J. Solid State Chem. 183 (2010) 2731–2738. doi:10.1016/j.jssc.2010.09.018.

[44] JCPDS reference n°04-017-216 (2014)

[45] Mgbemere, H. E., Hinterstein, M., & Schneider, G. A., Structural phase transitions and electrical properties of $(K_xNa_{1-x})NbO_3$-based ceramics modified with Mn, J. Eur. Ceram. Soc. 32, (2012) 4341-4352.

[46] P Mahesh and D Pamu, Raman and Dielectric Studies on Lead free $(K_{0.5}Na_{0.5})NbO_3$ Piezoelectric Ceramics, IOP Conference Series: Materials Science and Engineering, 73, (2015) 012141.

[47] W. Zhu, J. Zhu, M. Wang, B. Zhu, X. Zhu, G. Pezzotti, Raman tensor analysis of (K0.5Na0.5)NbO3-LiSbO3 lead-free ceramics and its application to study grain/domain orientation, J. Raman Spectrosc. 43 (2012) 1320.

[48] C. W. Ahn, H. J. Seog, A. Ullah, S. Y. Lee, J. W. Kim, S. S. Kim, M. Park, K. No, I. W. Kim, Effect of Ta content on the phase transition and piezoelectric properties of lead-free (K0.48Na0.48Li0.04)(Nb0.995-xMn0.005Tax)O3 thin film, J. App. Phys. 111 (2012) 024110.

[49] M. Polomska, B. Hilczer, M. Kosec, B. Malic, Raman scattering dtudies of lead free (1-x)K0.5Na0.5NbO3-xSrTiO3 relaxors, Ferroelectrics 369 (2008) 149.

[50] Mirza M. Shamim, T. Ishidate, K. Ohi, High pressure Raman study of KNbO3-KTaO3 and KNbO3-NaNbO3 mixed crystals, J. Phys. Soc. Jp 72 (2003) 551.

[51] X. Vendrell, J. E. Garcia, E. Cerdeiras, D. A. Ochoa, F. Rubio-Marcos, J. F. Fernandez, L. Mestres, Effect of lanthanide doping on structural, microstructural and functional

properties of K0.5Na0.5NbO3 lead-free piezoceramics, Ceramics International 42 (2016) 17530.

[52] J. Wang, L. Luo, The NbO6 octahedral distortion and phase structural transition of Eu3+-doped K0.5Na0.5NbO3-xLiNbO3 ferroelectric ceramics, J. Am. Ceram. Soc. (2017)1.

[53] S. Glinšek, D. Nuzhnyy, J. Petzelt, B. Malič, S. Kamba, V. Bovtun, M. Kempa, V. Skoromets, P. Kužel, I. Gregora, and M. Kosec, Lattice dynamics and broad-band dielectric properties of the KTaO3 ceramics, Journal of Applied Physics 111 (2012) 104101.

[54] C. H. Perry and T. F. McNelly, Ferroelectric soft mode in KTaO3, Phys. Rev. 154 (1967) 456.

[55] J. Kreisel, A. M. Glazer, P. Bouvier, G. Lucazeau, High pressure Raman study of a relaxor ferroelectric: The Na0.5Bi0.5TiO3 perovskite, Phys. Rev. B 63 (2001) 174106.

[56] H. –R. Xia, L. –X. Li, J. –Y. Wang, Y. –G. Liu, J. –Q. Wei, Soft-mode spectroscopy in Fe:KTa1-xNbxO3 crystals, Cryst. Res. Technol. 35 (2000) 1209.

[57] J. Petzelt, S. Kamba, J. Fabry, D. Noujni, V. Porokhonskyy, A. Pashkin, I. Franke, K. Roleder, J. Suchanics, R. Klein, G. E. Kugel, Infrared, Raman and high frequency dielectric spectroscopy and the phase transition in Na1/2Bi1/2TiO3, J. Phys.: Condens. Matter 16 (2004) 2719.

[58] Y. Amira, Y. Gagou, A. Menny, D. Mezzane, A. Zegzouti, M. Elaatmani, M. El Marssi, Structural and Raman properties of the tetragonal tungsten bronze ferroelectric Pb2(1-x)K1+xGdxNb5O15, Solid State Comm. 150 (2010) 419.

[59] D. Rout, K.-S. Moon, J. Park, S.-J. L. Kang, High-temperature X-ray diffraction and Raman scattering studies of Ba-doped (Na0.5Bi0.5)TiO3 Pb-free piezoceramics, Current Applied Physics 13 (2013) 1988.

[60] Lalitha K.V., L. M. Riemer, J. Koruza, J. Rödel, Hardening of electromechanical properties in piezoceramics using a composite approach , Appl. Phys. Lett. 111 (2017) 022905. doi :10.1063/1.4986911

[61] D. A. Hall, A. Steuwer, B. Cherdhirunkorn, T. Mori, and P. J. Withers, A high energy synchrotron x-ray study of crystallographic texture and lattice strain in soft lead zirconate titanate ceramics J. Appl. Phys. 96, (2004) 4245. Doi : 10.1063/1.1787590

[62] C. Bantignies, E. Filoux, R. Rouffaud, M. Pham Thi, P. Mauchamp, R. Dufait, J.-M. Grégoire, F. Levassort, Lead-free high-frequency linear-array transducer (30 MHz) for in vivo skin imaging, IEEE International Ultrasonics Symposium, Prague (2013) 785-788.

FIGURE CAPTIONS

Figure 1: XRD patterns of the $K_{0.5}Na_{0.5}Nb_{1-x}Ta_xO_3$ ceramics from x = 0 to x = 1. Insert: enlargement of the 45-46.5 °, corresponding to (202) and (020) diffraction peaks. Intensities have been intentionally shifted.

Figure 2: Evolution of the cell parameters as a function of x in $K_{0.5}Na_{0.5}Nb_{1-x}Ta_xO_3$, obtained from Rietveld refinements. All parameters are referred to the pseudo-cubic unit cell. Dashed lines are only guide to the eye.

Figure 3: (a) Room temperature Raman spectra of $K_{0.5}Na_{0.5}Nb_{1-x}Ta_xO_3$ ceramics for x = 0 to x = 1. (b) and (c) wavenumber as function of x for E_g (ν_2) and A_{1g} (ν_1) vibrations of the NbO_6 octahedra, respectively.

Figure 4: SEM images of $K_{0.5}Na_{0.5}Nb_{1-x}Ta_xO_3$ ceramics sintered by conventional sintering at 1120 °C - 10 h. (a) x = 0, (b) x = 0.05, (c) x = 0.10, (d) x = 0.20, (e) x = 0.50 and (f) x = 1.

Figure 5: SEM micrographs with backscattered electron detector of $K_{0.5}Na_{0.5}Nb_{1-x}Ta_xO_3$, sintered by conventional sintering (a) x = 0.05 and (b) x = 0.10, and sintered by spark plasma sintering (c) x = 0.05 and (d) (x = 0.10).

Figure 6: Relative densities for the whole range of x in $K_{0.5}Na_{0.5}Nb_{1-x}Ta_xO_3$ and for the two sintering techniques: ■ conventional sintering and ● spark plasma sintering.

Figure 7: SEM images with a backscattered electron detector of $K_{0.5}Na_{0.5}Nb_{1-x}Ta_xO_3$ (a) sintered by spark plasma sintering (x = 0.20), (b) zoom on junction between dark and clear inclusions and (c) zoom on the matrix area.

Figure 8: Evolution of K_p and d_{33} in $K_{0.5}Na_{0.5}Nb_{1-x}Ta_xO_3$ from x = 0 to x = 0.5, and for the two sintering techniques.

Figure 9: Electrical properties of $K_{0.5}Na_{0.5}Nb_{1-x}Ta_xO_3$ ceramics at room temperature for conventionally and SPS sintered compositions, from x = 0 to x = 0.5. ε_r and tanδ were measured at 1 kHz.

Table 1: Summary of the main electrical results of the SPS parameters study for x = 0.2 composition in $K_{0.5}Na_{0.5}Nb_{1-x}Ta_xO_3$.

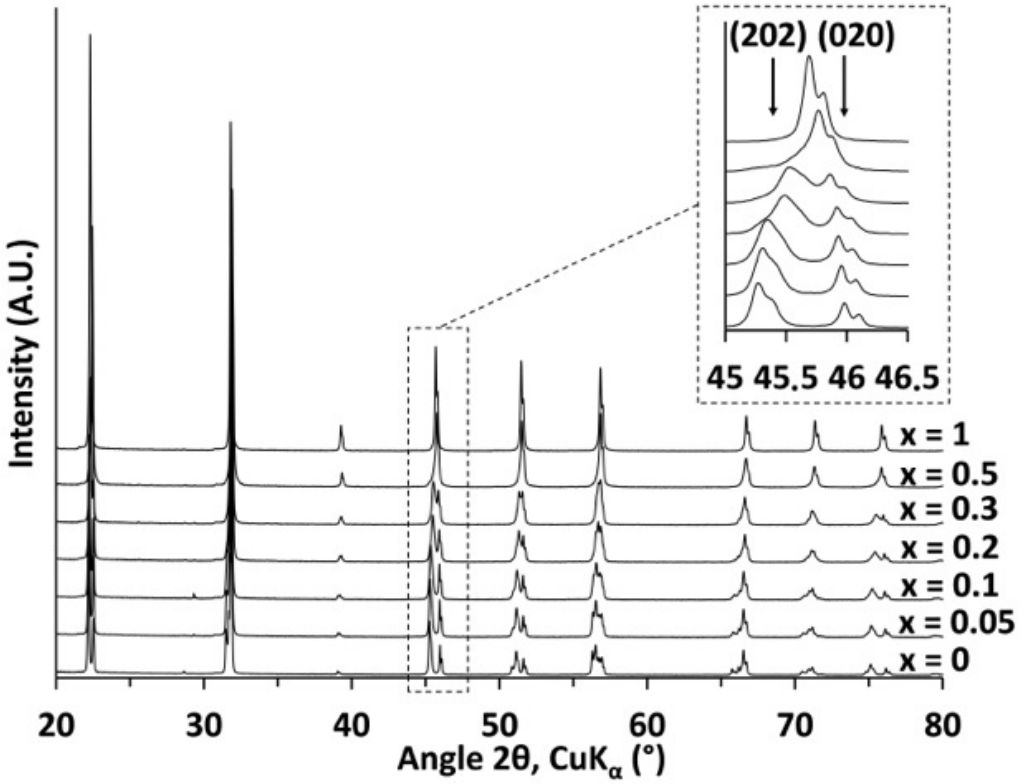
(202) (020)
45 45.5 46 46.5
Intensity (A.U.)
x = 1
x = 0.5
x = 0.3
x = 0.2
x = 0.1
x = 0.05
x = 0
20 30 40 50 60 70 80
Angle 2θ, CuK$_\alpha$ (°)

Fig.1

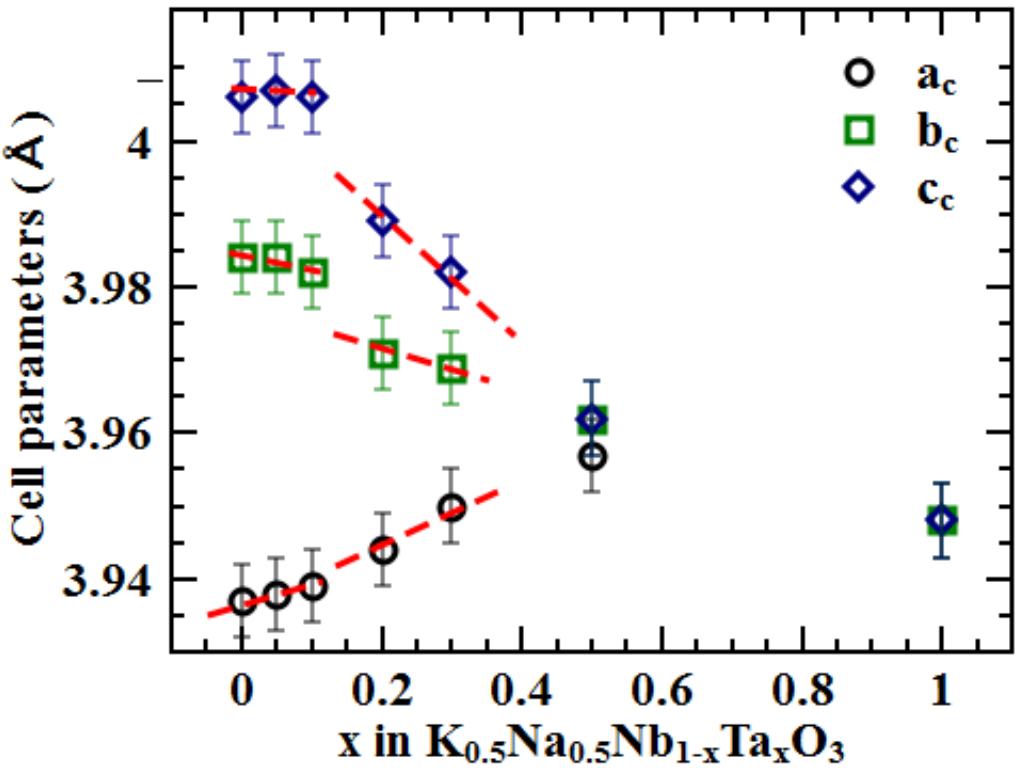
Cell parameters (Å)
4
3.98
3.96
3.94
a_c
b_c
c_c
0 0.2 0.4 0.6 0.8 1
x in $K_{0.5}Na_{0.5}Nb_{1-x}Ta_xO_3$

Fig.2

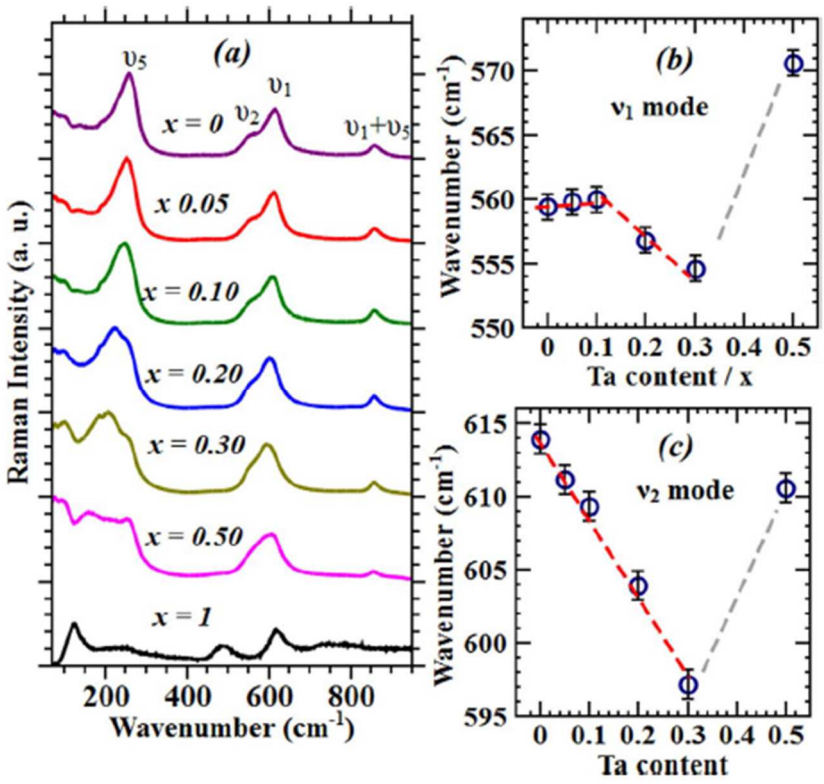
(a)
υ5
υ1
υ2
υ1+υ5
x = 0
x 0.05
x = 0.10
x = 0.20
x = 0.30
x = 0.50
x = 1
Raman Intensity (a. u.)
200 400 600 800
Wavenumber (cm-1)
(b)
ν1 mode
Wavenumber (cm-1)
570 565 560 555 550
0 0.1 0.2 0.3 0.4 0.5
Ta content / x
(c)
ν2 mode
Wavenumber (cm-1)
615 610 605 600 595
0 0.1 0.2 0.3 0.4 0.5
Ta content

Fig.3

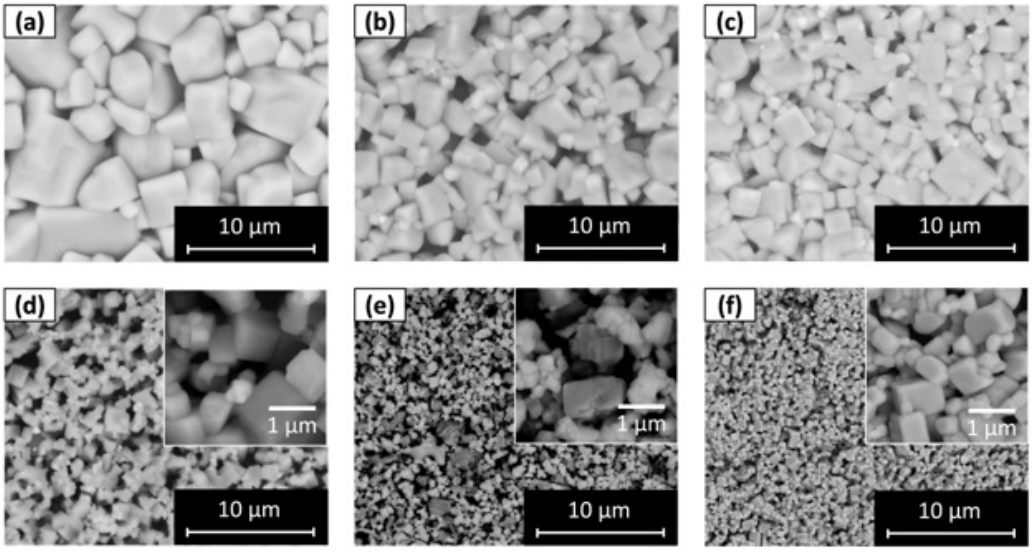
(a)
10 µm
(b)
10 µm
(c)
10 µm
(d)
1 µm
10 µm
(e)
1 µm
10 µm
(f)
1 µm
10 µm

Fig.4

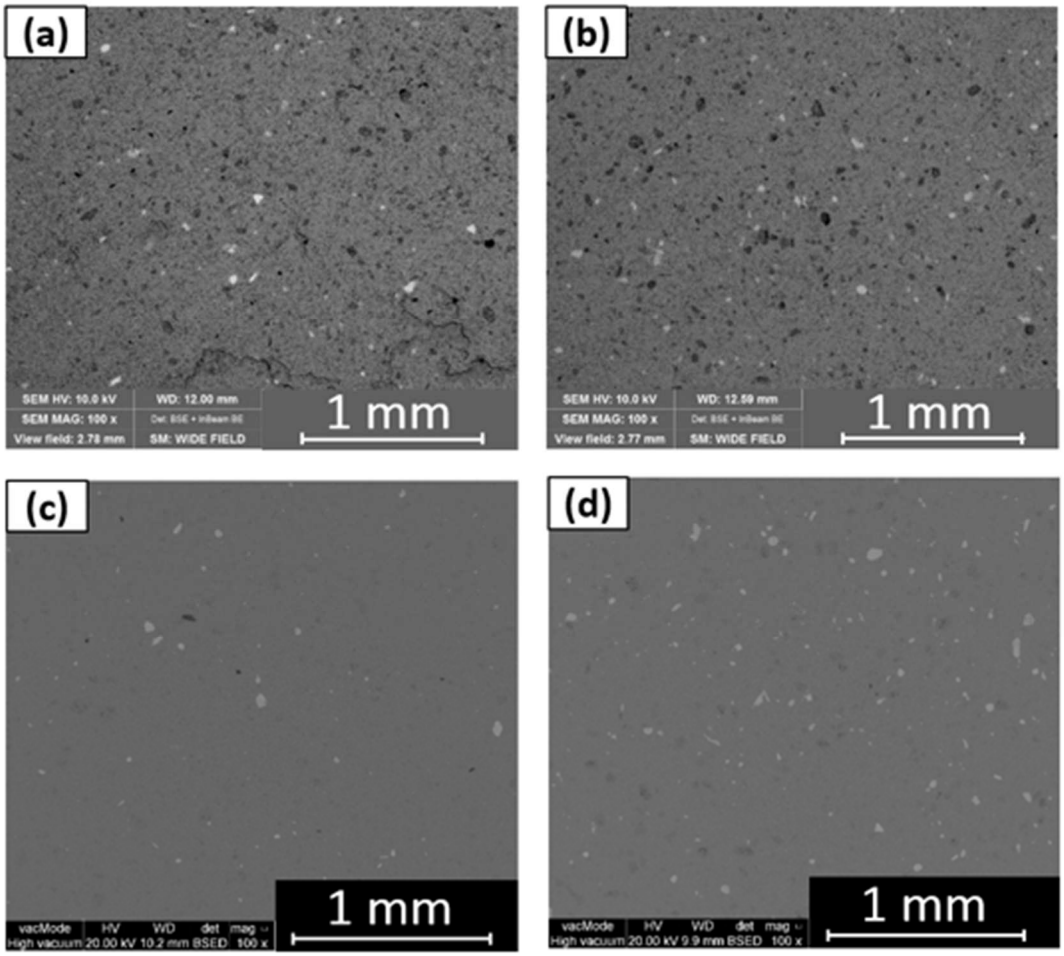
(a)
SEM HV: 10.0 kV
WD: 12.00 mm
SEM MAG: 100 x
Det: BSE + InBeam SE
View field: 2.78 mm
SM: WIDE FIELD
1 mm
(b)
SEM HV: 10.0 kV
WD: 12.59 mm
SEM MAG: 100 x
Det: BSE + InBeam SE
View field: 2.77 mm
SM: WIDE FIELD
1 mm
(c)
vacMode HV WD det mag
High vacuum 20.00 kV 10.2 mm BSED 100 x
1 mm
(d)
vacMode HV WD det mag
High vacuum 20.00 kV 9.9 mm BSED 100 x
1 mm

Fig.5

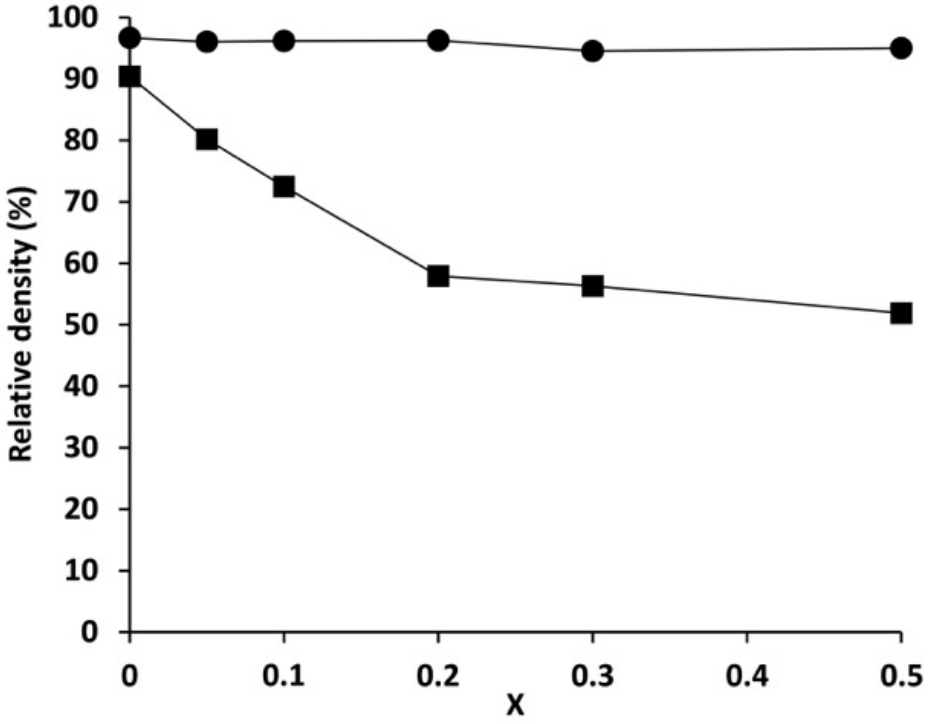
Relative density (%)
100
90
80
70
60
50
40
30
20
10
0
0
0.1
0.2
0.3
0.4
0.5
X

Fig.6

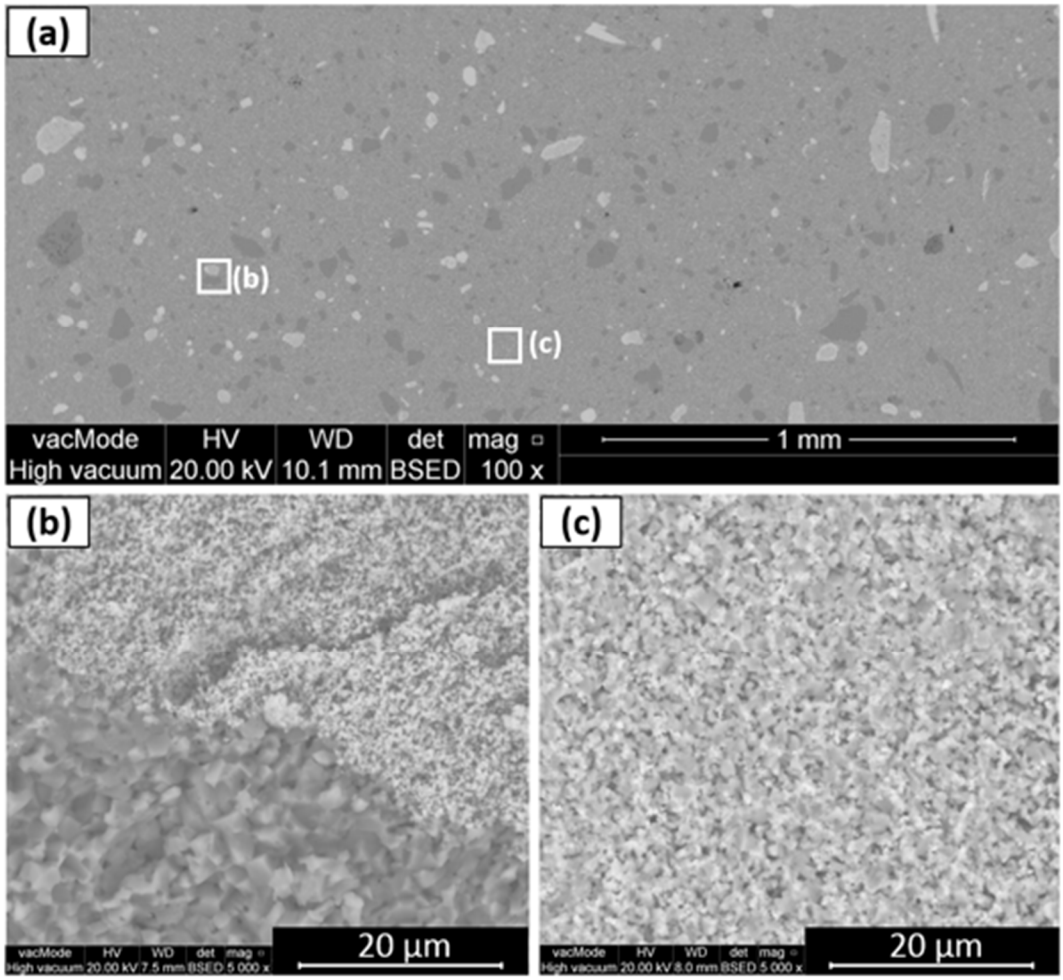
(a)
(b)
(c)
vacMode
High vacuum
HV
20.00 kV
WD
10.1 mm
det
BSED
mag
100 x
1 mm
(b)
20 µm
(c)
20 µm

Fig.7

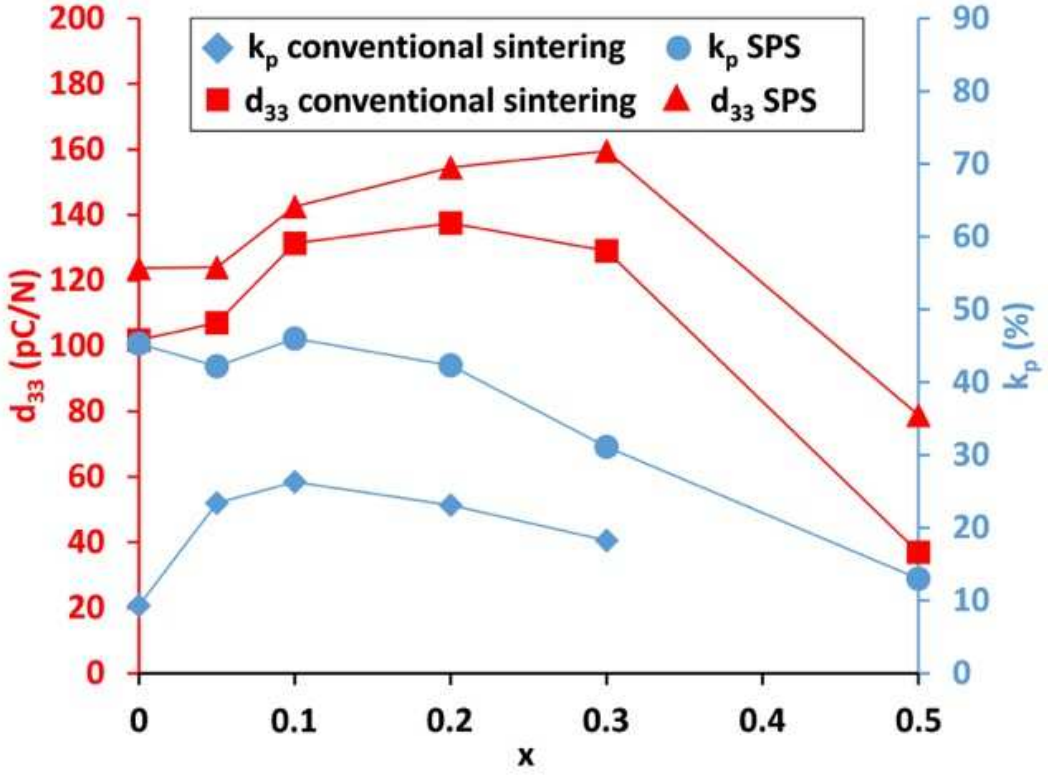
k_p conventional sintering
k_p SPS
d_33 conventional sintering
d_33 SPS
d_33 (pC/N)
k_p (%)
x
0
0.1
0.2
0.3
0.4
0.5
0
20
40
60
80
100
120
140
160
180
200
0
10
20
30
40
50
60
70
80
90

Fig.8

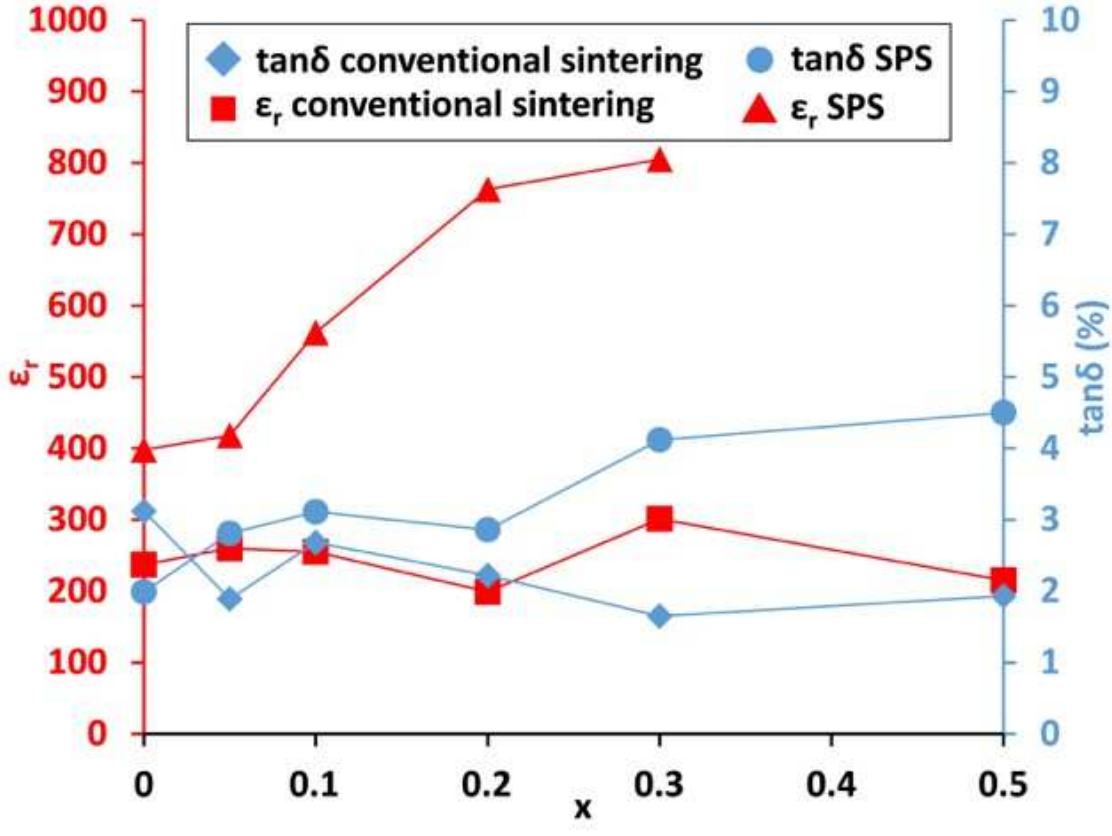
tanδ conventional sintering
tanδ SPS
ε_r conventional sintering
ε_r SPS
ε_r
tanδ (%)
x
0
0.1
0.2
0.3
0.4
0.5
0
100
200
300
400
500
600
700
800
900
1000
0
1
2
3
4
5
6
7
8
9
10

Fig.9

x	Ramp speed (°C/min)	Temperature (°C)	Dwell time (min)	Pressure (Mpa)	Relative density (%)	ε_r	tanδ (%)	d_{33} (pC/N)	k_p (%)
0.20	100	920	5	50	73.78	-	-	-	-
0.20	100	940	5	50	85.29	-	-	-	-
0.20	100	960	5	50	94.13	905	4.90	147.7	38.4
0.20	100	980	5	50	93.00	-	-	-	-
0.20	**50**	960	5	50	93.16	938	4.60	144.7	37.6
0.20	100	960	**10**	50	**96.25**	763	2.86	**154.5**	**42.3**
0.20	100	920	5	**200**	92.24	**1027**	5.41	135	35.0

Table 1